I&EC research
Industrial & Engineering Chemistry Research
pubs.acs.org/IECR
Article

Optimal Design of Solar Receivers in CSP Plants: Effects of Facility Location

José Antonio Luceño, Ester de la Fuente, and Mariano Martín*

Cite This: *Ind. Eng. Chem. Res.* 2021, 60, 7218–7231

ABSTRACT: This work presents a two-stage approach for the design and evaluation of the performance of solar central tubular receivers. First, the unit design is obtained using a mixed-integer nonlinear programing (MINLP) optimization problem, considering the radiation profile and the weather of the location. Later, with the design fixed, the NLP is solved to determine the performance of the receiver during a year. Three different locations are studied (Almería, Arizona, and Scotland), each of them with their characteristic radiation and weather. The designs obtained show the effect of the location on the size of the different elements of the receiver. The performance over a year presents the heat-transfer features as well as the effect of the wind speed profile affecting the convective heat transfer. The number of trade-offs results in the need for a comprehensive analysis for the design of these units toward reducing the pressure drop but considering the increase of the thermal stress on the tubes.

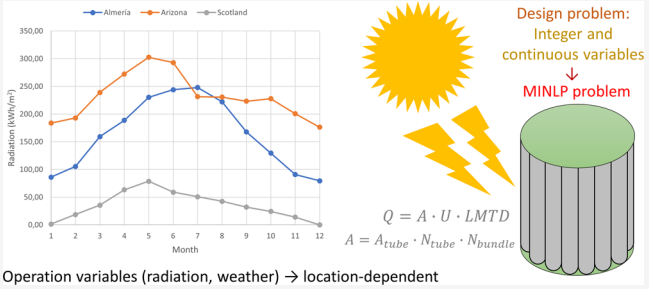

1. INTRODUCTION

Current society relies on electricity. Electricity, or electrical energy, is a key element for progress and development, increasing its demand with the growth of the population[1] or when new industries and technologies are developed, such as, data centers.[2] This form of energy can be obtained from the conversion of other sources, such as, combustion of fossil fuels (coal, gas, etc.), nuclear reactions, or employing renewable resources (wind, solar radiation, biomass, etc.). Renewable energies are the most interesting choice to produce electricity nowadays because they provide an alternative to increase the production of electricity[3] and represent the technologies that allow reducing greenhouse gas emissions.[4,5] Solar energy is the only energy source that the Earth receives, but it is more than enough to supply mankind needs. This work focuses on concentrated solar power (CSP) technologies that have received a lot of attention lately but still require additional development to improve the process efficiency to be installed across countries.[6] CSP technologies usually involve heat-transfer fluids (HTFs), used to capture solar energy for its use toward the production of energy via steam generation as well as a means to store thermal energy, enabling the overnight operation of the CSP plants.[7,8] HTFs are usually a mixture of two or more compounds; in previous works, molten salts[9] and synthetic fluids[10] were considered as HTFs.

CSP plants present three different sections: (1) the HTF circuit, which involves the heliostat field, the concentrating technology, and the thermal energy storage, if the facility has one of them; (2) the water−steam circuit, which comprises a heat exchanger network (to heat and evaporate the water stream) and a steam turbine (to produce electricity); and (3) the cooling system. There are different types of concentrating technologies, each one with a specific heliostat layout, but there are four main options nowadays: parabolic dish, parabolic trough, linear Fresnel reflector, and central receiver.[11−13] Section 2 is similar to traditional thermal power plants, where the difference is the use of HTFs and radiation to obtain the thermal energy employed to produce steam instead of the combustion of coal in a furnace. It consists of (1) a series of shell-and-tube heat exchangers to produce the steam and (2) high-, medium- and low-pressure turbines to generate electricity out of it.[13] Section 3 can present different cooling technologies, but in the case of CSP, there are two main technologies, wet cooling and dry cooling,[9,14,15] and an intermediate option (hybrid cooling).[16]

There are different designs of solar receivers, such as the open volumetric air receiver,[17−19] the porous cavity receiver,[20] the particle solar receiver,[21] and the central or tubular receiver.[22] Each technology has its own characteristics, such as the need to study the influence of critical parameters in porous cavity receivers to improve efficiency,[20] the analysis of different kinds of materials and its effect on the absorption in particle solar receivers,[21] or the importance of correct simulation of the return

Received: November 2, 2020
Revised: March 11, 2021
Accepted: April 15, 2021
Published: April 27, 2021

https://doi.org/10.1021/acs.iecr.0c05383
Ind. Eng. Chem. Res. 2021, 60, 7218−7231

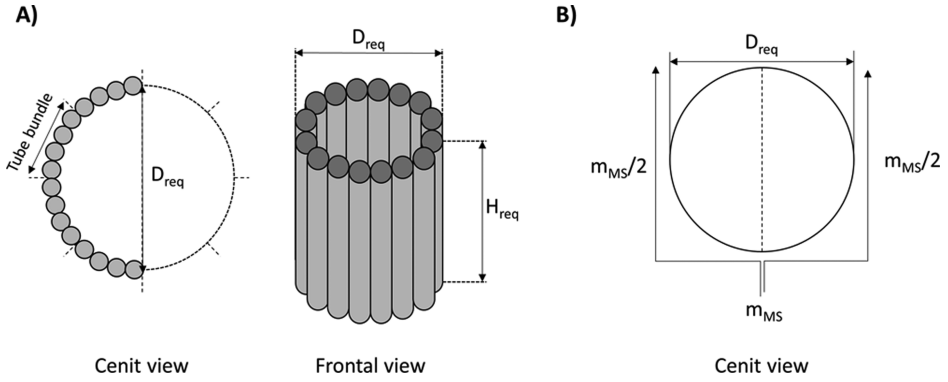

Figure 1. Central receiver scheme: (A) tube distribution and characteristic lengths; (B) flow splitting considered.

air flow chamber in open volumetric air receivers;[17] furthermore, some works use CFD modeling applied to the analysis and optimization for some technologies, such as porous volumetric receivers.[18] Each of these technologies have been studied by different authors, but in this work, the technology studied is the central tube receiver because it is the most used at a commercial scale.[22]

Previous studies presented design methodologies for this equipment,[23,24] the evaluation of the peak temperature that takes place on the tubes applying an optimization of fluid distribution,[25] the importance of a flux map calculus and an optimal distribution of the heliostat field to reduce thermal stress in the receiver,[26] the simultaneous lay out optimization of the central receiver (horizontal distribution) and heliostat field,[27] a methodology to control the energy reached by the receiver,[28] and even parametric studies about the design and operation of molten salt receivers.[29,30] However, most of the studies focused on the relative location of the receiver without paying that much attention to its purpose as a heat-transfer unit while the ones dealing with this aspect present a procedural and/or simulation-based design, where the effects of facility location on the design feature and its performance have not been reported in the literature. In addition, the various radiation profiles that the locations of the CSP facilities may present, results in the need for evaluating the effect of different facility locations, with different radiation and weather data, on the design and heat-transfer features of the receiver.

This work presents a two-step methodology for the optimal design and the evaluation of the performance of central tube receivers. In the first step, a mathematical formulation is developed for the sizing of the unit that simultaneously considers the trade-offs related to individual element sizing and layout. In a second step, the performance of the unit is evaluated over time. To address the location dependency on the unit design, different locations with their own weather data and two scenarios: same heliostat field (SHF) for all locations (resulting in different electricity production capacities) and different heliostat fields for each location [giving the same mean production (SMP) capacity] are evaluated. The receivers are optimally designed for each location and different scenarios. The work is organized in five sections: in the first section, the equations to design the equipment are presented; the second section deals with the framework used to design and evaluate each case; the third section presents the cases of study and the two scenarios and the value of some specific variables for the model; in the fourth section, the results are exposed and analyzed for both scenarios and cases. Finally, the conclusions of the work are drawn in section five.

2. MODEL FORMULATION

In this work, a central receiver CSP plant is considered. These facilities have a solar field surrounding a central structure, commonly a tower built with cement or iron,[31] on top of which the receiver is placed. The receiver is set considering that the entire external surface is exposed to solar radiation. Furthermore, the path of the HTF across the receiver will determine some design variables.[24]

The modeling section is divided into two main subsections. The first one is related to the detailed design of the receiver, considering three different aspects: mechanical design, thermal design, and pressure drop evaluation. Each section has its own subsections, where the equations used to calculate the design parameters of the unit are presented. The second subsection is focused on the study of the performance over time of the design obtained in the previous module.

2.1. Mechanical Design. The mechanical design comprises pipe selection, tower sizing, receiver design, and fluid flow path determination. It is recommended to choose the fluid flow path considering the hemisphere where the facility is located, in order to feed the fluid to the most convenient bundle, reducing the pressure drop and increasing the fluid velocity.[24] In this work, the consideration will be the same as previous work which recommends two parallel flow paths without considering which is the initial bundle,[32] in order to present a general design case.

2.1.1. Tube Selection. The tube external diameter (d_{ex}) and inner diameter (d_{in}) are selected according to standard sizes. In this work, the formulation used for the selection of the diameter of the pipe is presented in eqs 1−4.[33] Furthermore, the following sets of variables are introduced to simplify the nomenclature:

- number of external diameters is denoted $M = \{1,2,...,n_M\}$. It represents the number of external diameters that are considered as possible design values.
- number of internal diameters is denoted $J = \{1,2,...,n_J\}$. It corresponds to the number of possible internal diameters that are available for a specific M-external diameter. J can take different values across the set of external diameters.

$$d_{ex} = \sum_m d_{ex,m} \cdot y_{de,m} \qquad \forall\, m \in M \tag{1}$$

$$\sum_m y_{de,m} = 1 \qquad \forall\, m \in M \tag{2}$$

https://doi.org/10.1021/acs.iecr.0c05383
Ind. Eng. Chem. Res. 2021, 60, 7218−7231

$$d_{in} = \sum_{m}\sum_{j}(d_{in,j,m}\cdot y_{di,j,m}) \qquad \forall\, m, j \in M, J \tag{3}$$

$$\sum_{m}\sum_{j} y_{di,j} = 1 \qquad \forall\, m, j \in M, J \tag{4}$$

Typically, the values of the diameter considered for the design of heat exchangers are presented in TEMA standard diameter value tables.[34] For this case, a total of five different external diameters (d_{ex}) are considered, following the typical range of design.[24] Each external diameter has different inner diameter (d_{in}) combinations, between 4 and 10 choices of thickness, see Supporting Information. Only one diameter and one thickness must be selected.

In solar central receivers, the tube length, H_{req}, corresponds to the linear section that is exposed to solar radiation. The connections between bundles and inlet and outlet pipes are covered by a screen or a small wall;[35] meanwhile, the linear section is still exposed to the Sun. Thus, the tube length considered is usually the linear section (Figure 1a). In the model, the tube junctions are not considered as tube length; thus, the tube length (H_{req}) can be determined by the height-diameter ratio of the collector (HD_{ratio}), as eq 5,[24] where D_{req} is the diameter of the receiver (m); as a recommendation, the ratio HD_{ratio} should be between 1 and 2.[24]

$$HD_{ratio} = \frac{H_{req}}{D_{req}} \tag{5}$$

2.1.2. Tower Design and Rescaled Wind Speed. The tower height (H_{tower}) affects the value of wind speed and, as a result, the heat transfer. This height is employed to rescale wind speed literature data due to the dependence of the wind speed on the separation and the orography of the location.[36] In this work, eq 6 is used to estimate H_{tower}[24]

$$H_{tower} = 82.60 + 0.2552\cdot(Q_{req} \times 10^{-3}) \tag{6}$$

where Q_{req} is the required heat to be absorbed by the HTF molten salts (kW). For a given value of H_{tower}, the Hellman law equation, eq 7,[37] is employed to determine the wind speed value at the desired height

$$v_{Ht} = v_{meas}\cdot\left(\frac{H_{tower}}{H_{meas}}\right)^{\omega} \tag{7}$$

where v_{Ht} is the wind speed value at tower height (m/s), v_{meas} is the wind speed reported in the literature (m/s), H_{meas} is the height at which v_{meas} was measured (m), and ω is the friction coefficient or Hellman exponent. The ω value is tabulated, and it is a function of the ground topography. In this work, the value of 0.20 for ω was considered;[37] other values of ω can be consulted in Table S1 of the Supporting Information.

2.1.3. Receiver Design. The mechanical design of the receiver involves the definition of the geometry of the equipment. This geometry is related to the number of tubes that provide the contact area and guide the molten salts through the receiver. The areas involved are $A_{req,min}$, A_{flow}, A_{ob}, and A_{proj}.

The minimum total area required ($A_{req,min}$) can be determined according to the incoming irradiation and the maximum heat flow across the wall of the tubes, as shown in eq 8[24]

$$A_{req,min} = \frac{Q_{req}}{HF_{max}} \tag{8}$$

where HF_{max} is the maximum heat flow across tube wall (kW/m^2). The value of $A_{req,min}$ is the lower bound for the design area A_{ob} that must be satisfied during the entire cycle.

The flow section required across a tube bundle (A_{flow}) is obtained using eq 9, where n_{path} is the number of splits for the m_{MS}. In this work, it is considered that the molten salt stream is split in two streams, so each stream will go over the half receiver, and n_{path} is equal to 2 (Figure 1b).

$$A_{flow} = \frac{(m_{MS}/n_{path})}{\rho_{MS}\cdot v_{MS}} \tag{9}$$

where ρ_{MS} is the density (kg/m^3), m_{MS} is the total flow (kg/s), and v_{MS} is the velocity (m/s) of molten salts inside tubes (see Table S2 for the bounds).

The designed area (A_{ob}) and the projected area (A_{proj}) must be calculated using the design variables H_{req} and D_{req}, as shown in eqs 10 and 11[24]

$$A_{ob} = \pi\cdot\frac{\pi}{2}\cdot H_{req}\cdot D_{req} \tag{10}$$

$$A_{proj} = \pi\cdot H_{req}\cdot D_{req} \tag{11}$$

The value of D_{req} can be obtained from the layout of the tubes so that the entire bundle has enough area as presented in eq 12[23]

$$D_{req}\cdot\pi = N_{bundle}\cdot[B_{bundle} + B_{tube}\cdot(N_{tb} - 1) + N_{tb}\cdot d_{ex}] \tag{12}$$

where N_{bundle} is the number of bundles, B_{bundle} is the separation between bundles (m), B_{tube} is the separation between tubes (m), and N_{tb} is the number of tubes per bundle. The value of N_{tb} is determined starting using A_{flow} and the flow section of one tube, as seen in eq 13

$$N_{tb} = \frac{A_{flow}}{\frac{\pi}{4}\cdot(d_{in})^2} \tag{13}$$

As $n_{path} = 2$, the value of N_{bundle} must be an even number. This constraint can be satisfied considering that the rest of N_{bundle}/n_{path} must be an integer positive value. If it is required, this rest can be defined as an additional equation in the model, adding a new discrete variable.

2.2. Thermal Design of the Receiver. The thermal design of the equipment is focused on the variables that are involved in heat transfer, such as temperatures and heat flows.

2.2.1. Thermal Flows. The thermal design section presents the equations related to temperatures, fluid properties, dimensionless numbers, and heat-transfer coefficients. An energy balance to the molten salts is employed to determine the flow of molten salts required (m_{MS}), according to eq 14

$$Q_{req}\cdot\eta_{ther} = m_{MS}\cdot C_{p_{MS}}\cdot(T_{out} - T_{in}) \tag{14}$$

where η_{ther} is the thermal efficiency of the receiver, $C_{p_{MS}}$ is the specific heat [kJ/(kg·K)], T_{out} is the outlet temperature (K), and T_{in} is the inlet temperature (K) of the molten salts. The values of T_{in} and T_{out} are usually fixed depending on the HTF stability and flow properties, and m_{MS} changes each time period[9] so that the temperature of the molten salts stored is maintained over time. In this work, the values of T_{in} and T_{out} are taken to be 563.15 and 838.15 K, respectively, from previous works.[9,14]

Another important factor related to the operating temperatures is the heat flow across the tube wall (HF_{tube}). The tubes

https://doi.org/10.1021/acs.iecr.0c05383
Ind. Eng. Chem. Res. 2021, 60, 7218−7231

must be able to bear with the conduction heat transfer. The value of HF_{tube} can be determined using eq 15[24]

$$HF_{tube} = \frac{(m_{MS}/n_{path})\cdot C_{p_{MS}}\cdot \Delta T_{bundle}}{N_{tb}} \quad (15)$$

where ΔT_{bundle} is the temperature increment in each bundle (K), considering that it is equal in each bundle. It is computed using eq 16

$$\Delta T_{bundle} = \frac{(T_{out} - T_{in})}{(N_{bundle}/n_{path})} \quad (16)$$

HF_{tube} has to be lower than the maximum heat flow across tube wall used (HF_{max}, kW/m^2) for safety purposes and to ensure that tubes resist the thermal operating conditions. The value of HF_{max} is provided by the manufacturer. In the case of Incoloy steel, the value of HF_{max} is 1000 kW/m^2.[24] The constraint for HF_{max} is formulated as eq 17

$$HF_{tube} \le HF_{max}\cdot \pi \cdot H_{req}\cdot d_{ex} \quad (17)$$

HF_{tube} is involved in the calculation of the tube surface mean temperature [$\overline{T}_s$, (K)], as seen in eq 18

$$\overline{T}_s = \overline{T}_{MS} + HF_{tube}\cdot(R_{cond} + R_{conv}) \quad (18)$$

where $\overline{T}_{MS}$ is the molten salt mean temperature (K); this temperature is calculated as the average between the inlet and outlet molten salt temperature. R_{cond} is the heat resistance due to the conduction across the tube material (K/kW), and R_{conv} is the convection heat resistance of the HTF and the molten salts (K/kW). Thermal resistances can be determined using eqs 19 and 20

$$R_{cond} = \frac{\log(d_{ex}/d_{in})}{k_{tube}\cdot 2\pi \cdot H_{req}} \quad (19)$$

$$R_{conv} = \frac{1}{h_{in}\cdot d_{in}\cdot H_{req}\cdot \frac{\pi}{2}} \quad (20)$$

where k_{tube} is the thermal conductivity of the tube material [kW/((m^2/m)·K)] and h_{in} is the convective heat-transfer coefficient of the molten salts [kW/(m^2·K)]. The value of h_{in} can be calculated with eq 21, where the Nusselt number of the molten salts (Nu_{MS}) is determined using dimensionless numbers as shown in eqs 22−24[24]

$$h_{in} = \frac{Nu_{MS}\cdot k_{MS}}{d_{in}} \quad (21)$$

$$Nu_{MS} = 0.023\cdot(Pr_{MS})^{0.4}\cdot(Re_{MS})^{0.8} \quad (22)$$

$$Pr_{MS} = \frac{C_{p_{MS}}\cdot \mu_{MS}}{k_{MS}} \quad (23)$$

$$Re_{MS} = \frac{\rho_{MS}\cdot v_{MS}\cdot d_{in}}{\mu_{MS}} \quad (24)$$

where Pr_{MS} is the Prandtl number, μ_{MS} is the viscosity [kg/(m·s)], k_{MS} is the thermal conductivity [kW/((m^2/m)·K)], and Re_{MS} is the Reynolds number of the molten salts.

2.2.2. Thermal Efficiency. The thermal efficiency of the equipment (η_{therm}) is considered to obtain more accurate results. This efficiency is calculated as the ratio between the total energy received and the energy lost by heat-transfer mechanisms (Q_{loss} (kW)), as presented in eq 25.

$$\eta_{therm} = 1 - \frac{Q_{loss}}{Q_{req}} \quad (25)$$

The variable Q_{loss} can be determined applying eq 26, where $Q_{l.refl}$, $Q_{l.rad}$, and $Q_{l.conv}$ are the heat losses (kW) due to reflection, radiation, and convection mechanisms, respectively.

$$Q_{loss} = Q_{l.refl} + Q_{l.rad} + Q_{l.conv} \quad (26)$$

Each of their values are determined using a different set of equations:

- The reflection losses $Q_{l.refl}$ can be calculated considering a linear dependency with Q_{req}, as seen in eq 27. The receiver effective absorbance (α_{eff}) is determined with the receiver absorbance (α), as shown in eq 28; α is a characteristic of the chosen material. In this case, a value of 0.95 is considered.[24]

$$Q_{l.refl} = (1 - \alpha_{eff})\cdot Q_{req} \quad (27)$$

$$\alpha_{eff} = \frac{\alpha}{\alpha + (1 - \alpha)\cdot \frac{\pi}{2}} \quad (28)$$

- The radiation losses $Q_{l.rad}$ are calculated applying the expression for radiation transfer, as seen in eq 29

$$Q_{l.rad} = \sigma_{SB}\cdot \varepsilon_{eff}\cdot A_{proj}\cdot(\overline{T}_s^4 - \overline{T}_{env}^4) \quad (29)$$

where σ_{SB} is the Stefan−Boltzmann constant [$5.6704\cdot10^{-11}$ kW/(m^2·K^4)], ε_{eff} is the receiver effective emissivity, and $\overline{T}_{env}$ is the mean atmospheric temperature (K). As in the case of α_{eff}, ε_{eff} can be determined with the receiver emissivity ε using eq 30. Furthermore, the value ε is material-dependent, and it is also affected by the tube coating chosen. In this work, ε values are estimated by a $\overline{T}_s$-based function obtained using literature data,[35] as seen in eq 31, where temperature T is introduced in K.

$$\varepsilon_{eff} = \frac{\varepsilon}{\varepsilon + (1 - \varepsilon)\cdot \frac{\pi}{2}} \quad (30)$$

$$\varepsilon = 3.5746 \times 10^{-7}\cdot(T^2) - 1.0557 \times 10^{-4}\cdot(T) + 2.7008 \times 10^{-1} \quad (31)$$

- The convection losses $Q_{l.conv}$ are determined using eq 32, which shows the usual convection transfer expression

$$Q_{l.conv} = h_{mix}\cdot A_{ob}\cdot(\overline{T}_s - \overline{T}_{env}) \quad (32)$$

where h_{mix} is the heat-transfer coefficient for mixed convection (kW/m^2·K). The mixed convection involved two kinds of mechanisms, natural convection (characterized by h_{nat} transfer coefficient) and forced convection (characterized by h_{for} transfer coefficient). The value of h_{mix} can be calculated using eq 33

$$h_{mix} = (h_{nat}^{\ m} + h_{for}^{\ m})^{1/m} \quad (33)$$

where the coefficient m is scalar which is fixed beforehand according to the receiver type; its value is between 3 and 4.[35] For an external receiver such as the one in this case study, the value of m is 3.2.[35] The coefficients h_{nat} and h_{for} are computed from the Nusselt number for natural convection and forced convection, respectively, as seen in eqs 34 and 35, where k_{air} is the thermal conductivity of air [kW/((m^2/m)·K)].

https://doi.org/10.1021/acs.iecr.0c05383
Ind. Eng. Chem. Res. 2021, 60, 7218−7231

$$h_{nat} = \frac{Nu_{nat} \cdot k_{air}}{H_{req}} \tag{34}$$

$$h_{for} = \frac{Nu_{for} \cdot k_{air}}{D_{req}} \tag{35}$$

Each Nu number is computed using an empirical correlation, and it depends on the flow regime. In the case of natural convection, in addition to Reynolds and Prandtl numbers, two additional dimensionless numbers are required such as Grashof (Gr_{air}) and Rayleigh (Ra_{air}) numbers. These last dimensionless numbers are calculated using eqs 36 and 37

$$Gr_{air} = \frac{g \cdot \beta_{air} \cdot (\overline{T}_s - \overline{T}_{env}) \cdot H_{req}^{\ 3}}{\kappa_{air}^{\ 2}} \tag{36}$$

$$Ra_{air} = Gr_{air} \cdot Pr_{air} \tag{37}$$

where β_{air} is the volumetric expansion coefficient (K^{-1}), κ_{air} is the kinematic viscosity (m^2/s), and Pr_{air} is the Prandtl number of air, which is determined with an analogous expression than eq 23. In order to use, eqs 37 and 38 must be satisfied[23]

$$\frac{D_{req}}{H_{req}} \geq \frac{35}{Gr_{air}^{\ 0.25}} \tag{38}$$

Using the values of Pr_{air} and Ra_{air}, the Nusselt number for natural convection (Nu_{nat}), for turbulent flow, can be estimated using eq 39.[38] The Nusselt number for forced convection (Nu_{for}) is calculated using eq 40, where Re_{air} is the Reynolds number of air.

$$Nu_{nat} = \left[0.825 + \frac{0.387 \cdot Ra_{air}^{\ 1/6}}{\left(1 + \left[\frac{0.492}{Pr_{air}}\right]^{9/16}\right)^{8/27}} \right]^2 \tag{39}$$

$$Nu_{for} = 0.0455 \cdot (Re_{air})^{0.81} \tag{40}$$

The equations used to predict the heat-transfer coefficients are reported to provide a good estimation within the operating range according to the literature where the fitting was obtained.[38] By using the same model for different cases, the comparison is consistent so that the differences should not be ascribed to the equations used to estimate them.

2.3. Pressure Drop. The pressure drop is a core point for the design of the equipment because a lower pressure drop usually means lower operating costs. The energy consumed to overcome pressure drop must be provided using pumps. The pressure drop ΔP_{tot} is estimated considering the tube pressure drop, and the pressure drop is given by the tower height, as seen in eq 41

$$\Delta P_{tot} = \Delta P_{receiver} + \Delta P_{tower} = \Delta P_{tube} \cdot N_{bunSec} + \Delta P_{tower} \tag{41}$$

where $\Delta P_{receiver}$ is the receiver pressure drop (Pa), ΔP_{tube} is the pressure drop across one tube (Pa), N_{bunSec} is the number of bundles per receiver section, and ΔP_{tower} is the pressure drop associated to the tower (Pa).

- ΔP_{tower} can be estimated using eq 42

$$\Delta P_{tower} = \rho_{MS} \cdot g \cdot H_{tower} \tag{42}$$

- ΔP_{tube} is determined with eqs 43 and 44, considering different design variables, such as the fanning factor (f), the rugosity of tubes (in this work, it is considered as stainless steel $\zeta = 0.2 \cdot 10^{-5}$ m[39]), H_{req} and d_{in}, or flow variables, such as Reynolds number of the molten salts (Re_{MS}) and ν_{MS}. The curvature length of tubes (inlet and outlet connections) is not considered, in order to follow the same assumption presented for H_{req}.

$$\Delta P_{tube} = \rho_{MS} \cdot f \cdot \frac{H_{req}}{d_{in}} \cdot \frac{\nu_{MS}^{\ 2}}{2} \tag{43}$$

$$\frac{1}{\sqrt{f}} = -2 \cdot \log\left(\frac{\frac{\zeta}{d_{in}}}{3.7} + \frac{2.51}{Re_{MS} \cdot \sqrt{f}} \right) \tag{44}$$

The power consumption of the pumps (W_{pump}) can be determined employing eq 45, where V_{MS} is the volumetric flow of molten salts (eq 46) (m^3/s) and η_{pump} is the pump efficiency, which is assumed to be 0.8.

$$W_{pump} = \frac{\Delta P_{tot}}{\eta_{pump}} \cdot V_{MS} \tag{45}$$

$$V_{MS} = \frac{m_{MS}}{\rho_{MS}} \tag{46}$$

To evaluate the tradeoff between the operating costs, related to pumping the fluid, versus the global heat-transfer coefficient including the conduction across the pipe and the heat flux that a pipe can hold and the investment cost of the selection of the unit, we consider limited number of external diameters, 5 d_{ex}, from 4 to 10 thicknesses within the TEMA standard.[24]

2.4. Objective Function. The objective function (Z) consists of three different items: (1) the annualized equipment capital cost; (2) the operating costs; and (3) the influence of more efficiency operation. The equipment capital cost was estimated considering the volume of the material [V_{st} (m^3)], which is calculated as shown in eq 47. The operating costs are related to the pump energy consumption, which can be estimated using the pressure drop, as shown in eq 45. The influence of efficiency was taken into account considering a hypothetical production of the energy not captured by the unit. The part of the total energy not produced by the plant, Q_{loss}, should be obtained using nonrenewable sources, such as coal, which will generate CO_2 emissions: the more efficient the unit is, the lower the amount of emissions produced will be. Thus, a penalty to lower efficiencies can be introduced in the objective function using as variable Q_{loss}. Thus, the objective function is given by eq 48

$$V_{st} = \frac{\pi}{4} \cdot (d_{ex}^{\ 2} - d_{in}^{\ 2}) \cdot H_{req} \cdot N_{tb} \cdot N_{bundle} \tag{47}$$

$$Z = \frac{(V_{st} \cdot \rho_{st} \cdot C_{st})}{K_{rec} \cdot EL_{rec}} + W_{pump} \cdot \left(744 \frac{kWh}{kW \cdot month}\right) \cdot C_{elec} + Q_{loss} \cdot \left(744 \frac{kWh}{kW \cdot month}\right) \cdot EP_{CO_2} \cdot C_{CO_2} + C_{area} \cdot \Delta area \tag{48}$$

where ρ_{st} is the density (kg/m^3) and C_{st} is the cost of the material of the tube ($/kg), EL_{rec} is the time considered for amortization purposes (year), K_{rec} is the number of months considered for

https://doi.org/10.1021/acs.iecr.0c05383
Ind. Eng. Chem. Res. 2021, 60, 7218−7231

amortization purposes (month/year), C_{elec} is the cost of electricity ($/kWh), EP_{CO_2} is the equivalent production of CO_2 if the energy was obtained from nonrenewable sources (kg CO_2/kWh), C_{CO_2} is the cost of CO_2 per kg ($/kg CO_2), C_{area} is the penalty value for nonused area [$/($m^2$·month)], assumed to be 2000 $/($m^2$·month), and Δarea is the difference between the value of A_{ob} and $A_{req,min}$ (m^2). The value of EL_{rec} considered was 30 years old, based on literature data.[35,40] The value of C_{elec} is estimated considering that the energy would be supplied by the CSP plants; thus, C_{elec} = 0.16 $/kW h.[9] The values of EP_{CO_2} and C_{CO_2} are estimated using mean values of previous reports: in the case of EP_{CO_2}, the value is considered according to the estimation of United Nations, EP_{CO_2} = 0.632 kg CO_2/kWh;[41] the value of C_{CO_2} is usually autoassigned by the companies themselves to consider the CO_2 footprint as a cost for its production, and a mean value could be C_{CO_2} = 40 $/kg CO_2.[42] The values of Incoloy steel variables are collected from different sources: the value of ρ_{st} is 7950 kg/m^3,[43,44] meanwhile, the value of C_{st} is 25 $/kg.[45]

The objective function for the second stage of the model is the same as eq 48 but with fixing design variables (i.e., the first term and the A_{ob} value inside the Δarea term). This equation enables us to consider the fluctuation of production and weather and radiation variable for each month and also the corresponding amortization of the equipment.

3. SOLUTION PROCEDURE

CSP facilities are sized at a design point.[8,9] However, the performance must be evaluated over a year. The solution procedure for the design of units operating under variable resources results in large nonlinear nonconvex mixed-integer nonlinear programming (MINLP) problems. Several works are presented in the literature to solve MINLP formulations applied to solar applications, such as energy supply superstructures.[46] However, in the case of unit design, nonlinearities involved in the estimation of heat-transfer coefficients, pressure drop, fanning factor, and so forth., including logarithms, ratios, power exponents, and fractions of the previous ones, present additional challenges. Therefore, in this work, we presented a two-stage approach to address the problem.[14] In the first stage, the equipment is designed for the scenario that presents the most demanding conditions; this first stage corresponds to a MINLP problem. Using the results of the design problem, in the second stage, a new nonlinear programming (NLP) problem is formulated to study one-year time horizon.

The design problem, an MINLP, consists of 111 continuous variables and 46 discrete variables involved in a total of 74 equations. The equations applied are the ones presented in Section 2. The upper bounds and lower bounds for the design variables are collected in Table S2. Since the design problem is an MINLP, different nonlinear solvers are used for a multistart optimization procedure. Once the design is fixed, the model is reformulated to study the one-year performance using historic data. The thermal storage of the CSP plant mitigates short time variability in the operation, and therefore, monthly discretization is assumed. Control of the operation is out of the scope of the work. In this case, the same equations of the first stage are applied, but a majority of design variables are fixed (such as diameters, areas, number of tubes, etc.). The variables related to heat transfer and flows (i.e., heat-transfer coefficients, Reynolds numbers, air mass flow, molten salt flow, etc.) are reformulated as monthly dependent variables: $h_{for} \rightarrow h_{for}(m)$; this reformulation implies an increase in the number of variables due to their dependence on the time period. The following list presents the variables that should be reformulated as monthly depended variables: Q_{req}, v_{MS}, m_{MS}, η_{ther}, $\overline{T}_s$, HF_{tube}, R_{conv}, h_{in}, Nu_{MS}, Re_{MS}, Q_{loss}, $Q_{l.refl}$, $Q_{l.rad}$, $Q_{l.conv}$, T_{env}, Gr, Ra, Nu_{nat}, h_{nat}, Nu_{for}, h_{for}, h_{mix},ΔP_{tube}, f, ΔP_{tot}, W_{pump}, and Z. The NLP monthly performance problem presents a total of 511 constraints, which are divided into 24 inequalities and 487 equations, with a total of 487 variables involved if the plant operates 12 months.

4. CASES OF STUDY

In this work, three different locations are considered in order to study the effect of different weather and radiation conditions in the design and its effects in heat transfer. The locations selected are Almería (Spain), Arizona (USA), and Scotland (UK).

The three locations present different mean profiles of wind velocity (Figure S1, in Supporting Information) and also different ranges of values. Scotland has the highest values and a curved profile; Almería shows semioscillating values around 4.5 m/s, being the second higher value interval; finally, Arizona presents a constant mean value (2.8 m/s). The atmospheric temperature (Figure S2) follows the same profile in all locations, but there is a larger difference between the lowest and highest temperature in Arizona (around 20 K), followed by Almería (close to 15 K) and Scotland (around 12 K).

The profiles of radiation are also very different from one case to the other. In this work, direct normal irradiation, DNI, was used to characterize the radiation (Figure S3). First, it can be observed that there is a large difference between the radiation profile of Scotland and that of Arizona or Almería. Scotland's DNI follows a monotonic positive tendency until April, and later, the trend becomes negative. Almería presents a profile that has larger values during summer and spring months and lower during autumn or winter, describing a curve with the minimum value in December and the highest in July. The case of Arizona also shows a similar profile, but the yearly variation is smaller.

Furthermore, two scenarios will be studied for each location: (a) SHF scale, which results in different mean productions, and (b) SMP, which involves different plant sizes. These scenarios shed light into the effect of production capacity and weather characteristics in the values of heat-transfer variables: comparing and presenting a range of variable values at different weather (SMP scenario) and variation of values due to larger production at the same location (SHF). The mean production in the SMP scenario will be calculated considering only the operating months: if a case does not operate for 12 months, the mean production will be determined with a lower number of months. This approach is applied in order to not overdesign the receiver.

4.1. General Data and SHF Scenarios. The data related to weather and radiation conditions are the inputs that the model requires for the design of the receiver. In particular, the essential data for the present model are wind speed, atmospheric temperature, and DNI data, which are presented in Figures S1−S3 of the Supporting Information. These raw data need a previous processing to be employed on the model:

(1) the values of Q_{req} must be determined for each month and scenario; and

(2) the wind speed data must be rescaled according to the procedure of eqs 6 and 7 using Q_{req} values. The Q_{req} data were determined using eq 49

https://doi.org/10.1021/acs.iecr.0c05383
Ind. Eng. Chem. Res. 2021, 60, 7218−7231

$$Q_{req} = \frac{DNI \cdot A_{heli} \cdot (\eta_{heli}) \cdot d_{month}}{d_{month} \cdot h_{sun}} \quad (49)$$

where DNI is the mean direct normal irradiation of the month considered [kWh/(m^2·d)], A_{heli} is the area of heliostat field (m^2), η_{heli} is the efficiency of heliostat field, d_{month} is the number of days of the month (d), and h_{sun} is the number of sun hours with enough irradiation (h). Some of these variables can be fixed according to the following points:

- η_{heli} was assumed to be 0.90.
- A_{heli} value must be the same in the SHF scenario, and the value chosen was 317,880 m^2, as previous works.[9]

The h_{sun} value was calculated comparing the hourly DNI data of a typical day, for each location and month,[47] with the minimum radiation threshold, which was considered 250 W/m^2;[48] the values of h_{sun} and d_{month} are collected from an institutional data base.[47] The values of Q_{req} for each location, for SHF scenarios, are plotted in Figure 2, and the wind speed data

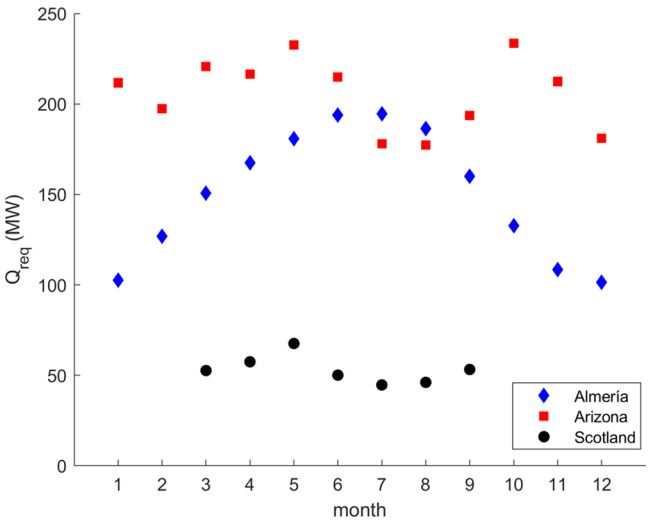

Figure 2. Q_{req} data for each location (SHF scenario).

rescaled are collected in Supporting Information (see Figure S4). In Figure 2, it can be seen that each location shows a different energy availability profile and range of values. Furthermore, due to the constraint on the radiation threshold (250 W/m^2), the Scotland profile presents 5 months below the radiation threshold; thus, these months cannot be considered to operate the thermodynamic cycle.

The profile of Q_{req} is location dependent. In the case of Arizona, the fluctuation is small and around a mean value of 205 MW, presenting the highest values of the three locations. In the case of Scotland, the energy absorbed shows low fluctuation, but the mean value is 53 MW, presenting the lowest value of all locations. Oppositely, the case of Almería shows a profile with the largest fluctuation during the year, due to the weather of the region, presenting a range of values between 100 and almost 200 MW, with a mean value of around 150 MW. These three cases allow a comprehensive study for the effect of the radiation profile on the design and on the heat-transfer variables.

4.2. SMP Scenarios. To study the second scenario, where the facilities have the SMP capacity in MW at every location, the value of A_{heli} must be rescaled to provide the energy required. In this work, the rescaling of A_{heli} is performed using the mean annual production values of each location ($MV_{location}$); these values are calculated considering the operating months for each location. Later, the largest mean production value (MV_{LV}) between all locations is defined, and a correction factor for each location ($CF_{location}$) is calculated according to eq 50. The $MV_{location}$ and $CF_{location}$ results are collected on Table 1; the rescaled Q_{req} data are plotted on Figure 3, and the new wind speed data are represented on Figure S5.

$$CF_{location} = \frac{MV_{LV}}{MV_{location}} \quad (50)$$

Table 1. Correction Factors for the SMP Case

location	Almería	Arizona	Scotland
$MV_{location}$ (MW)	150.46	205.83	53.12
$CF_{location}$	1.37	1.00	3.87

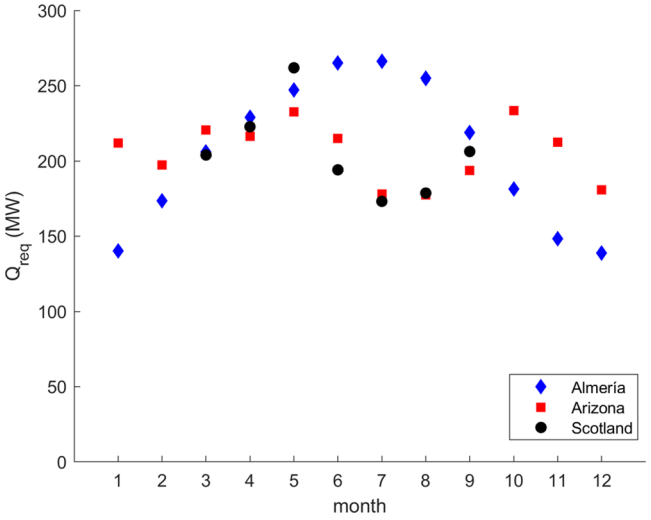

Figure 3. Q_{req} data rescaled for each location (SMP scenario).

In Figure 3, the data corresponding to Almería data are above the ones from Arizona, which is the opposite case with respect to the SHF scenario; this is due to the fact that Almería presents larger seasonal variability, with lower values during autumn and winter months, and it must be offset with higher values during summer and spring. Scotland's data are close to Arizona's data, with minor differences in spring-early summer months in order to offset the value of May.

5. RESULTS

In this section, the results obtained for the different locations are presented in two subsections. Section 5.1 compares different designs for the three locations and two plant sizes while in section 5.2, the performance of the designs under various scenarios are presented.

5.1. Receivers Designs. The first step consists of the design of the optimal receiver according to the characteristics of the location. Inputs of the weather and radiation data are required (see Section 4). The model described in Section 2 is solved as an MINLP for each location. Following the design criteria of considering the most demanding operating condition, each location has a different design month, but this month will be the same for both scenarios, SMP and SHF. According to Figure 2, the design months considered for equipment design in the cases of Almería, Arizona, and Scotland were July, October, and May,

https://doi.org/10.1021/acs.iecr.0c05383
Ind. Eng. Chem. Res. 2021, 60, 7218−7231

Table 2. Receiver Design for Each Scenario and Location

	Almería		Arizona		Scotland	
variable	SHF	SMP	SHF	SMP	SHF	SMP
H_{req} (m)	7.265	7.473	7.344	7.344	4.087	7.675
D_{req} (m)	5.429	7.219	6.446	6.446	4.087	7.675
A_{ob} (m^2)	194.629	266.240	233.609	233.609	82.435	290.694
A_{proj} (m^2)	123.905	169.494	148.72	148.72	52.45	185.062
H_{tower} (m)	132.269	150.544	142.217	142.217	99.851	149.439
d_{ex} (m)	0.022	0.032	0.032	0.032	0.022	0.025
d_{in} (m)	0.020	0.030	0.030	0.030	0.020	0.024
A_{flow} (m^2)	0.029	0.040	0.035	0.035	0.010	0.039
N_{tb}	88	56	50	50	30	88
N_{bundle}	8	12	12	12	14	10
$n_{tubeTOT}$	704	672	600	600	420	880
B_{tube} (m)	0.002	0.002	0.002	0.002	0.008	0.002
B_{bundle} (m)	0.002	0.002	0.002	0.002	0.010	0.002

respectively. In Table 2 the most important variables of the receiver design are presented for each location for both two scenarios: SHF and SMP.

As expected, higher values of Q_{req} result in the need for a larger unit. The total area can be increased by a larger number of tubes or longer and wider tubes. The solution is not straightforward. In the case of Arizona, both scenarios present the same values because the production rate is the same; thus, there is no difference in the receiver design. Almería and Scotland cases present changes on the designs due to the need for rescaling the heliostat field.

In the case of Almería, the increased production capacity from SHF to SMP results in the use of larger tubes (slightly longer and 33% larger D_{req}) and 33% larger diameter of the pipes (d_{in} and d_{ex} increase) but in a lower amount of the total number of tubes ($n_{tubeTOT}$), one-third less per bundle. This fact can be explained comparing the increase in the value of A_{ob} against the value required for the SHF scenario (37% higher). Furthermore, the value of A_{flow} increases with respect to the SHF scenario because of the larger d_{in}, close to 38%. This can be justified based on eq 13, where the effect of increasing d_{in} is higher than decreasing N_{tb}. The values of B_{tube} and B_{bundle} show that the tubes have the same split in both scenarios, which indicates that the increase in the values of D_{req} and A_{proj} is related to the different distribution of tubes in a larger value of N_{bundle}, according to eq 12. The new larger value of H_{tower} is also related to the larger production capacity, as seen in eq 6.

The case of Scotland is similar to the one presented for Almeria. The SMP scenario requires a far larger unit compared to the one required under the SHF. The tubes employed in the SMP scenario have around double the length (H_{req}) and larger flow area A_{flow}, close to 4 times larger, due to the change in N_{tb}. These changes in the design of the tubes and the notable increase of the number of tubes, $n_{tubeTOT}$, result in an increase in the value of A_{ob} close to 3.5 times that obtained for the SHF scenario. The large difference in A_{ob} is directly related to the $CF_{location}$ value of Scotland (see Table 1) because Scotland is a region with low solar radiation and even a noncontinuum production (see Figure 2); thus, the heliostat field expansion should be larger than Almeria's case. In this case, B_{tube} and B_{bundle} show different values in each scenario, which was lower in the SHF case. This reduction can be related with D_{req} and $n_{tubeTOT}$ because the increase of D_{req} is slightly lower than that of the number of tubes, $n_{tubeTOT}$ (close to twice larger, vs, more than twice larger) and also with the increment in the tube diameter in the SMP case. Larger and more tubes are needed as well as with a smaller separation between them. The larger value of H_{tower} in the SMP scenario has the same explanation than the one presented for Almería's case, the larger value of Q_{req}.

If the three SMP scenarios are compared, the general rule is that the total production does not only define the geometry of the receiver but also that it is not possible to establish a range of values for the variables, considering Q_{req} due to the number of trade-offs in terms of area needs and power consumption, which makes the mathematical formulation a powerful tool for the design of the receiver. However, changing the value of HF_{max} has a notable effect of design variables values; an example with the value HF_{max} = 465 kW/m^2 is presented in Supporting Information Table S3. The reduction of HF_{max} implies larger units because the design is more conservative.

5.2. Unit Performance. In this section, the most important results obtained after the study of the three locations' performance are presented. More information about convective heat-transfer coefficients is reported in the Supporting Information (Tables S4−S6).

Figure 4 presents the evolution of m_{MS} and h_{in} during a year. For all locations, it can be observed that the m_{MS} values follow the same tendency as the radiation in that particular place, but in the SMP case, the variation is larger than in the SHF case for Almería (Figure 4a) and Scotland (Figure 4c). This variation is closely related to the $CF_{location}$ value (Table 1). Furthermore, there are subtle differences between the scenarios of each location. These differences can be related to the value of A_{flow} and its discontinuous nature as a result of the standard diameter sizes. A larger change of A_{flow} results in a more notable alteration in the profile of m_{MS}. Even though the variable that determines the profile of m_{MS} is the solar radiation, these results show that the design may also have an effect on the operating variables. The comparison between m_{MS} and h_{in} in Figure 4 shows that there is a direct relationship between their profiles, as expected. Close to the same, h_{in} values are obtained in SMP and SHF scenarios for each location. It can be due to the fact that the range of values of eq 21 is mainly determined by d_{in}, and the variation of Nu_{MS} describes the tendency of data.

The changes in η_{therm} with m_{MS} were also studied. They are presented in Figure 5. In all locations, the variation of η_{therm} between both scenarios is lower than or close to 1% and presents the same profile as m_{MS}. Furthermore, it can be noticed that the case of Arizona (Figure 5b) achieves the highest values of η_{therm}, considering SMP and SHF cases of Almería (Figure 5a) and

https://doi.org/10.1021/acs.iecr.0c05383
Ind. Eng. Chem. Res. 2021, 60, 7218−7231

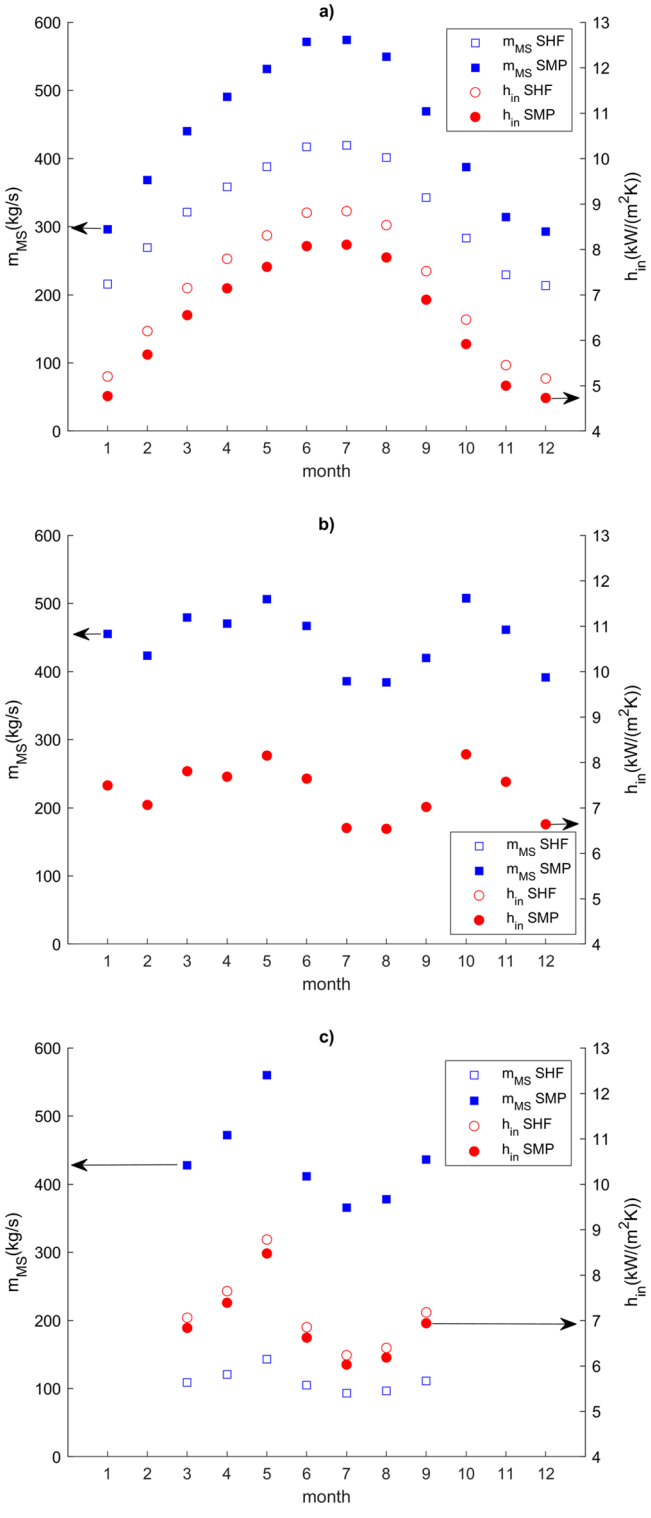

Figure 4. Fluctuation of salt flow and h_{in} during a year for each location and for both scenarios: (a) Almería; (b) Arizona; and (c) Scotland.

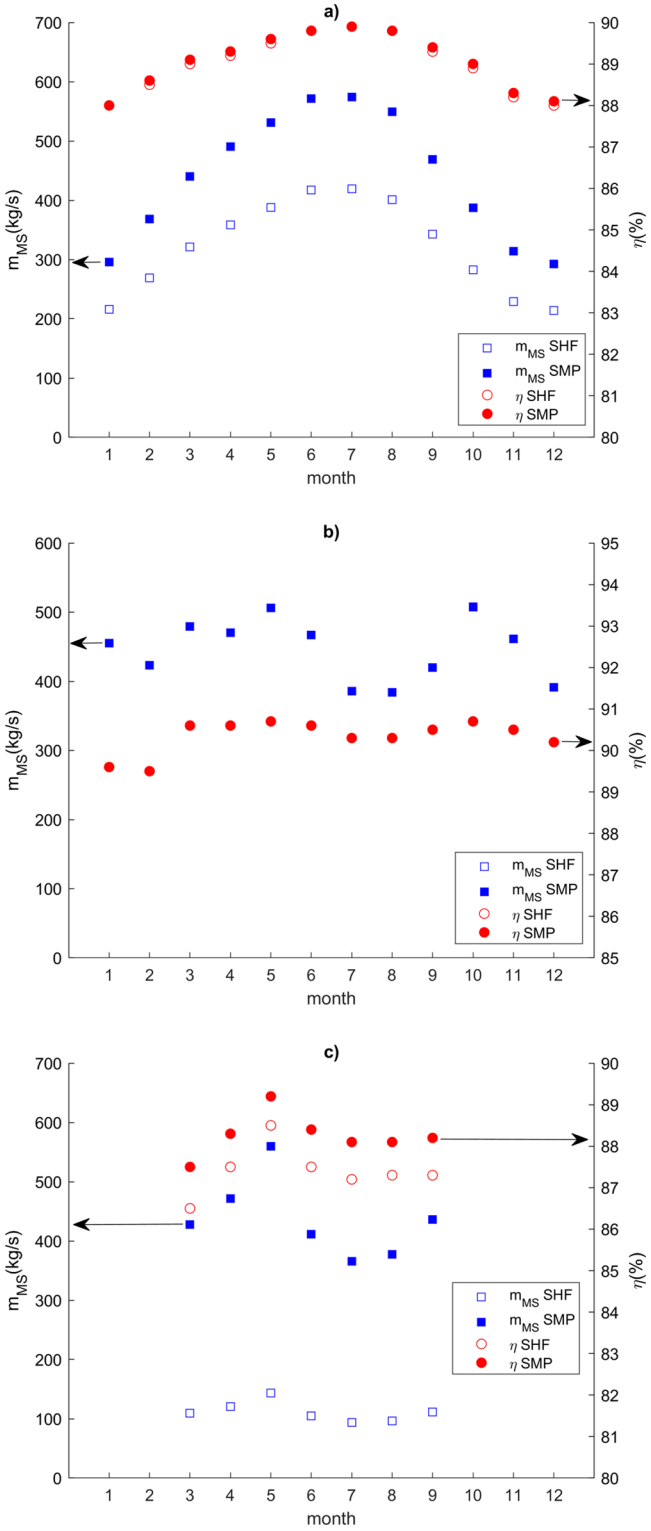

Figure 5. Fluctuation of salt flow and efficiency during a year for each location and both scenarios: (a) Almería; (b) Arizona; and (c) Scotland.

Scotland (Figure 5c). It means that the rescaling of Q_{req} does not affect so much η_{therm}, but the radiation profile is a key factor to achieve larger efficiencies. As a result, it can be said that the lower the fluctuation in radiation, the higher the η_{therm} is reached.

Evaluating the contributions of thermal losses (Figure 6), it can be observed that reflection losses represent the largest decrease in the efficiency, above half of the total losses [approx. Arizona—75% (Figure 6b), Almería—65% (Figure 6a), Scotland—60% (Figure 6c)]. As eq 27 is linearly depended on Q_{req}, the radiation represents around 10% or less of the losses in all cases. However, the larger the mean ambient temperature ($\bar{T}_{env}$), the larger the radiation losses in that location, which can explain the increase of the contribution of $Q_{l,rad}$ to the total Q_{loss}. This temperature could also affect $Q_{l,conv}$, but the effect of the

https://doi.org/10.1021/acs.iecr.0c05383
Ind. Eng. Chem. Res. 2021, 60, 7218−7231

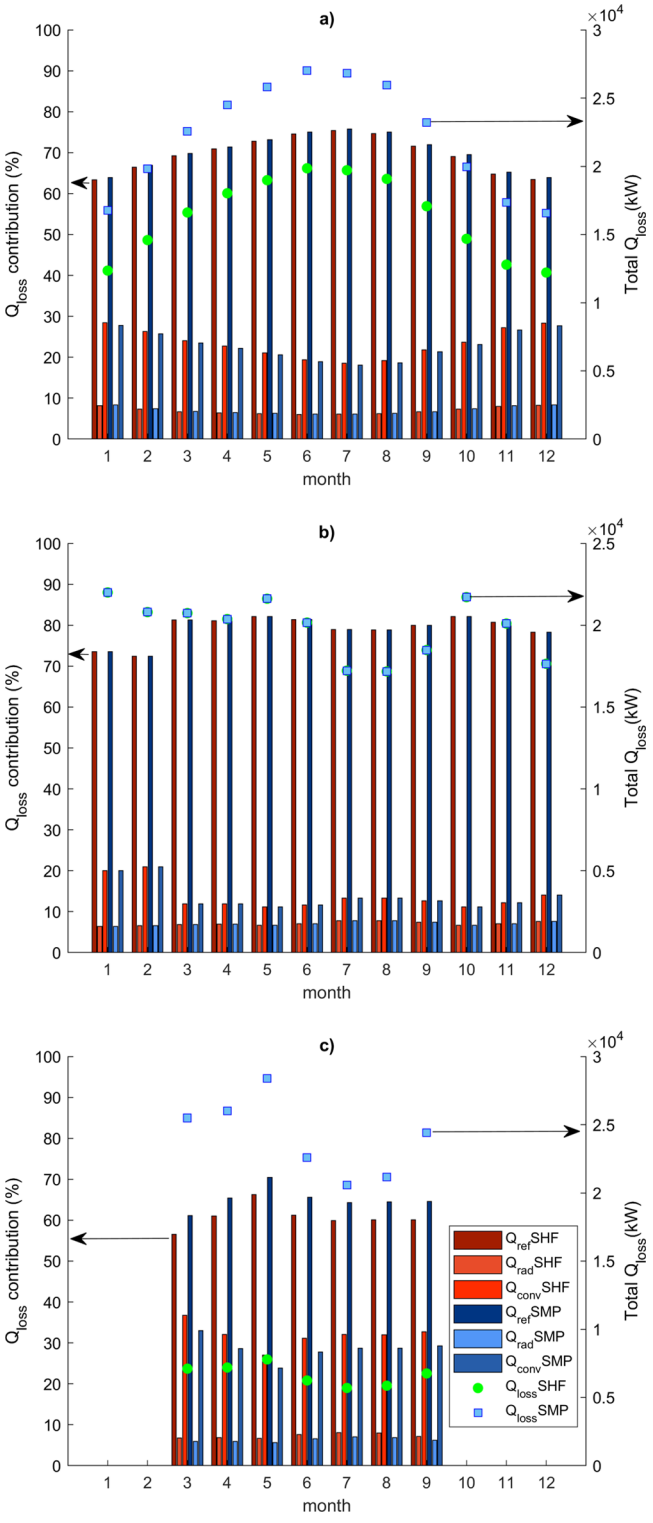

Figure 6. Contribution of each thermal loss mechanism during a year for each location and both scenarios: (a) Almería; (b) Arizona; and (c) Scotland.

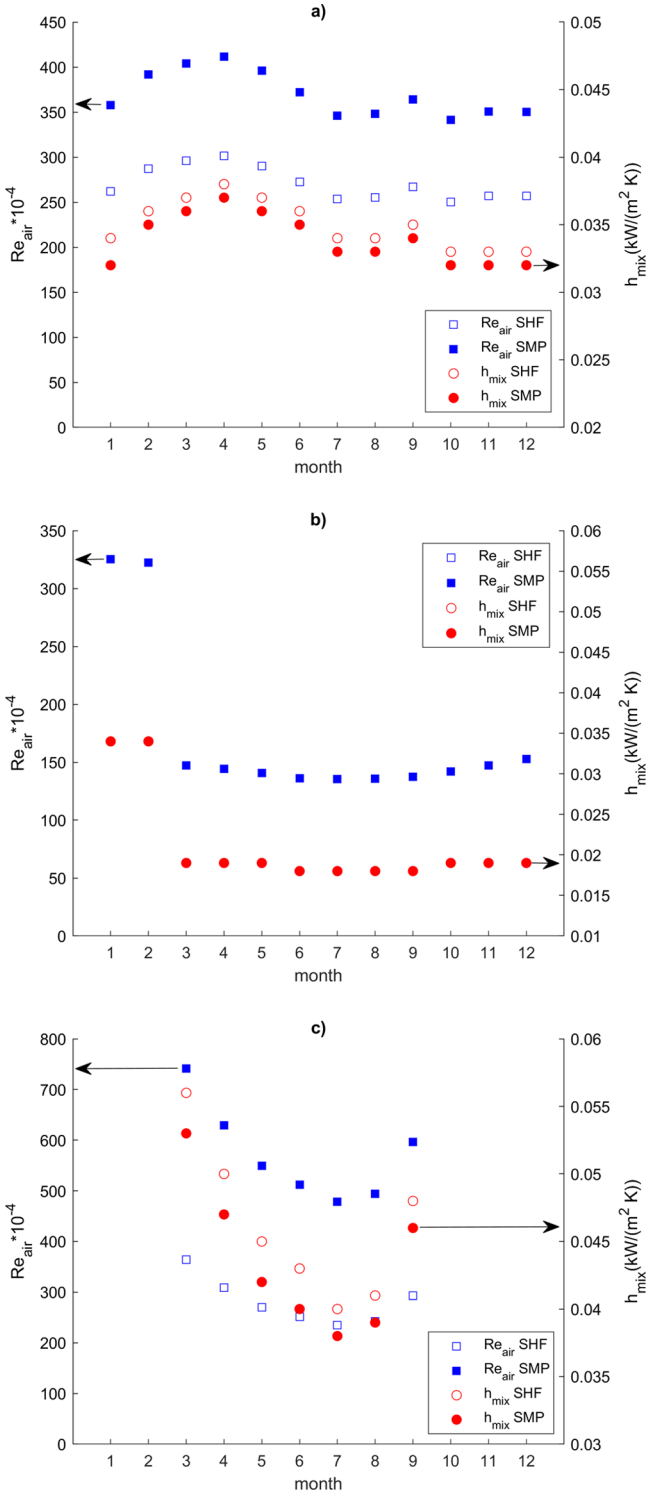

Figure 7. Fluctuation of $Re_{air} \times 1 \times 10^{-4}$ and h_{mix} during a year for each location and both scenarios: (a) Almería; (b) Arizona; and (c) Scotland.

wind (studied by Re_{air}) is more important, as seen in the values of h_{mix} in Figure 7. h_{mix} has a direct dependence with Re_{air}, and the values are mostly the same in both scenarios, SMP and SHF, for each location. The range of values and profile are determined by the wind speed (which affects Re_{air}). Note that the nonrescaled minimum velocities range from 2 to 6 m/s (Arizona location), while the maximum velocities range from 5 to 10 m/s (Scotland location), see Figure S1, which are twice the ones of the previous location. As wind speed is lower [Arizona scenario (Figure 7b)], h_{mix} presents values 30−50% lower than other locations, Almeria (Figure 7a) and Scotland (Figure 7c), which shows the effect of the weather conditions (wind) on the convective heat transfer. Looking at Tables S5−S7, the contribution of h_{mix} (h_{nat} and h_{for}) can be compared. For all cases, the value of h_{nat} is close to 1×10^{-2}; meanwhile, h_{for} is higher (except to Arizona scenario

https://doi.org/10.1021/acs.iecr.0c05383
Ind. Eng. Chem. Res. 2021, 60, 7218−7231

because from March, both values are similar), so the value of h_{mix} is very close to h_{for}.

Another variable that is affected by m_{MS} is ΔP_{tube}, which is shown in Figure 8. First, weather conditions affect the ΔP_{tube}

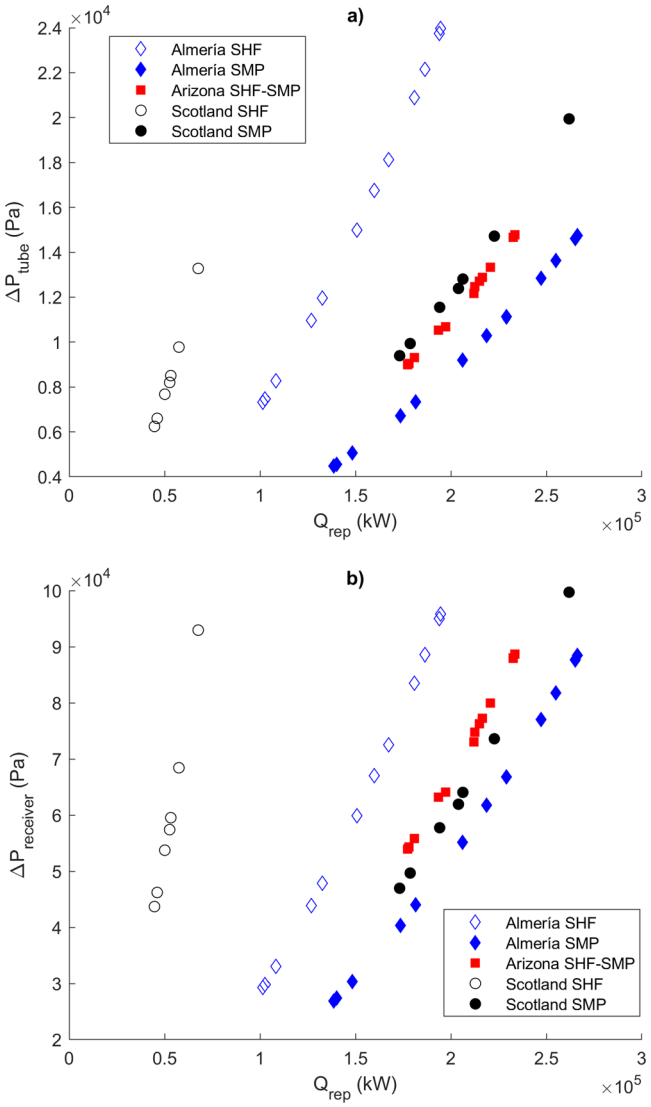

Figure 8. Fluctuation of pressure drop and Q_{req} during a year for each location and both scenarios: (a) tube pressure drop and (b) receiver pressure drop (considering bundles).

profile in all locations, as seen in Figure S6. However, the comparison of ΔP_{tube} between locations shows that there is no relationship with m_{MS} because the ΔP_{tube} increment is not proportional to the corresponding increase of m_{MS}. These variations are related to the design of the receiver. In Figure 8, the pressure drop is presented versus Q_{req}. In Figure 8a, SHF scenarios show higher values of ΔP_{tube} than SMP ones and also a larger interval of values in the case of Scotland. However, the analysis of the results must consider the different receiver design (Table 2). This comparison is presented in Figure 8b. SMP scenarios show lower $\Delta P_{receiver}$ values than SHF scenarios for the same Q_{req}. This is due to the distribution of tubes: a larger n_{tubbun} and lower n_{bundle} results in lower $\Delta P_{receiver}$. The reduction of $\Delta P_{receiver}$ is an option to increase the viability of the equipment, due to the decrease of W_{pump}, but a trade-off with the heat transfer across the tube wall has to be achieved. A lower n_{bundle} implies that ΔT_{bundle} could be larger and also HF_{tube}; the tubes bundles must operate with a value HF_{tube} lower than $HF_{TA,max}$.

6. CONCLUSIONS

This work develops a two-stage strategy for the design of central tubular solar receivers to simultaneously consider the number of trade-offs involved in the selection of size and tube layout. It allows evaluating the effect of the location of the facility on both the sizing of the units and on the operating variables. The location affects the design due to the effect of variables such as weather conditions, radiation profile, or even water availability. The optimal design and the performance are formulated as a two-step procedure, where first, the equipment is designed applying a MINLP, and later, the study of the performance is approached as an NLP.

Three locations were considered: Almería (Spain), Arizona (USA), and Scotland (UK). Each of them has a different radiation profile, operation period, and weather so that the comparison between them presents useful information about design tendencies and heat-transfer behavior. Furthermore, two different scenarios were considered for each location: SHF (different mean production) and SMP. The design results show larger power production and larger units. However, the particular sizing of the elements is location dependent. The increment of area is attributed to larger tubes, in general, but to a lower amount of tubes in the case of Almería. However, the total production does not define the geometry of the receiver.

The operating results provide useful information on how these receivers work. The study shows that the heat-transfer coefficient, h_{in}, follows the same profile than m_{MS} for each location and scenario, depending on the value of the inner diameter. The variation of η_{therm}, which depends on m_{MS}, is lower than 1% for all locations and scenarios; furthermore, higher radiation profile values and higher efficiencies are seen. The thermal losses correspond mainly to the reflection mechanism (65−75%) and second to the convection mechanism, being less important radiation losses due to the work temperature (close to 10%). Finally, the evolution of $\Delta P_{receiver}$ is related with the number of bundles and tube per bundle that the design has: larger bundles (more tubes) and lower $\Delta P_{receiver}$; however, it implies that the thermal stress of the tube could be larger. The variability of solar and wind velocities presents the opportunity to develop algorithms and solution procedures to include two-stage stochastic programming in the design of heat transfer.

■ ASSOCIATED CONTENT

Supporting Information

The Supporting Information is available free of charge at https://pubs.acs.org/doi/10.1021/acs.iecr.0c05383.

Friction coefficient values; upper bounds and lower bounds of variables; design results; contribution of *hnat* and *hfor* in *hmix*; wind speed data; temperature of the environment; direct normal irradiation; rescaled wind speed data; and fluctuation of pressure drop (PDF)

■ AUTHOR INFORMATION

Corresponding Author

Mariano Martín − *Departamento de Ingeniería Química y Textil, Universidad de Salamanca, 37008 Salamanca, Spain;* orcid.org/0000-0001-8554-4813; Email: mariano.m3@usal.es

https://doi.org/10.1021/acs.iecr.0c05383
Ind. Eng. Chem. Res. 2021, 60, 7218−7231

Authors

José Antonio Luceño − *Departamento de Ingeniería Química y Textil, Universidad de Salamanca, 37008 Salamanca, Spain;* orcid.org/0000-0003-0695-2689

Ester de la Fuente − *Departamento de Ingeniería Química y Textil, Universidad de Salamanca, 37008 Salamanca, Spain*

Complete contact information is available at: https://pubs.acs.org/10.1021/acs.iecr.0c05383

Notes

The authors declare no competing financial interest.

■ ACKNOWLEDGMENTS

The authors want to acknowledge Salamanca Research for optimization software licenses and PSEM3 research group for computer availability.

■ NOMENCLATURE

d_{ex}	external tube diameter (m)
d_{in}	internal tube diameter (m)
M	set of external diameter options
n_M	number of external diameter options
J	set of internal diameter options
n_J	number of internal diameter options
m	m-element of M
j	j-element of J
$y_{de,m}$	binary variable of m-external diameter option
$y_{di,j,m}$	binary variable of mj-external diameter option
HD_{ratio}	relation between the height and the diameter of the receiver (m)
H_{req}	receiver height (m)
D_{req}	receiver diameter (m)
H_{tower}	tower height (m)
Q_{req}	required heat to be absorbed by molten salts (kW)
v_{Ht}	wind speed value at tower height (m/s)
v_{meas}	wind speed (m/s)
H_{meas}	height where v_{meas} was measured (m)
ω	friction coefficient or Hellman exponent
$A_{req,min}$	minimum total area required (m^2)
HF_{max}	maximum heat flow across the tube wall (kW/m^2)
A_{flow}	flow section required across a tube bundle (m^2)
n_{path}	number of splits for molten salt flow
ρ_{MS}	density of molten salts (kg/m^3)
m_{MS}	total flow of molten salts (kg/s)
v_{MS}	velocity of molten salts inside tubes (m/s)
A_{ob}	designed area (m^2)
A_{proj}	projected area (m^2)
N_{bundle}	number of bundles
B_{bundle}	separation between bundles (m)
B_{tube}	separation between tubes (m)
N_{tb}	number of tubes per bundle
η_{ther}	thermal efficiency of the receiver
$C_{p_{MS}}$	specific heat of molten salts [kJ/(kg·K)]
T_{out}	outlet temperature of molten salts (K)
T_{in}	inlet temperature of molten salts (K)
HF_{tube}	heat flow across the tube wall (kW)
ΔT_{bundle}	temperature increment in each bundle (K)
$\overline{T}_s$	tube surface mean temperature (K)
$\overline{T}_{MS}$	molten salt mean temperature (K)
R_{cond}	heat resistance due to the conduction of tubes (K/kW)
R_{conv}	convection heat resistance of molten salts (K/kW)
k_{tube}	thermal conductivity of tubes [kW/((m^2/m)·K)]
h_{in}	convective heat-transfer coefficient of molten salts [kW/(m^2·K)]
Nu_{MS}	Nusselt number of molten salts
Pr_{MS}	Prandtl number of molten salts
μ_{MS}	viscosity of the molten salts [kg/(m·s)]
k_{MS}	thermal conductivity of the molten salts [kW/((m^2/m)·K)]
Re_{MS}	Reynolds number of the molten salts
Q_{loss}	energy lost by heat-transfer mechanisms (kW)
$Q_{l.refl}$	heat losses due to reflection mechanism (kW)
$Q_{l.rad}$	heat losses due to radiation mechanism (kW)
$Q_{l.conv}$	heat losses due to convection mechanism (kW)
α_{eff}	receiver effective absorbance
α	receiver absorbance
σ_{SB}	Stefan−Boltzmann constant [kW/(m^2·K^4)]
ε_{eff}	receiver effective emissivity
$\overline{T}_{env}$	mean atmospheric temperature (K)
ε	receiver emissivity
h_{mix}	heat-transfer coefficient for mixed convection (kW/m^2·K)
h_{nat}	heat-transfer coefficient for natural convection (kW/m^2·K)
h_{for}	heat-transfer coefficient for forced convection (kW/m^2·K)
m	scalar of receiver type mix convection transfer
k_{air}	thermal conductivity of air [kW/((m^2/m)·K)]
Nu_{nat}	Nusselt number for natural convection
Nu_{for}	Nusselt number for forced convection
Gr_{air}	Grashof number of air
Ra_{air}	Rayleigh number of air
β_{air}	volumetric expansion coefficient of air (K^{-1})
κ_{air}	kinematic viscosity of air (m^2/s)
Pr_{air}	Prandtl number of air
ΔP_{tot}	total pressure drop (Pa)
ΔP_{tube}	pressure drop across one tube (Pa)
N_{bunSec}	number of bundles per receiver section
ΔP_{tower}	pressure drop associated to the tower (Pa)
g	gravity acceleration (m/s^2)
f	fanning factor
ζ	rugosity of tubes (m)
W_{pump}	power consumption of pumps (kW)
V_{MS}	volumetric flow of molten salts (m^3/s)
η_{pump}	pump efficiency
V_{st}	volume of Incoloy steel (m^3)
Z	objective function ($/month)
ρ_{st}	density of the material of the tube (kg/m^3)
C_{st}	cost of the material of the tube ($/kg)
ELrec	time assigned to amortization purpose (year)
K_{rec}	number of months considered for amortization purpose (month/year)
C_{elec}	cost of electricity ($/kWh)
EP_{CO_2}	equivalent production of CO_2 if the energy was obtained from non-renewable sources (kg CO_2/kWh)
C_{CO_2}	cost of CO_2 per kg ($/kg CO_2)
C_{area}	penalty value for non-used area [$/(m2·month)]
Δarea	difference between the value of A_{ob} and $A_{req,min}$ (m^2)
$\Delta P_{receiver}$	total pressure drop through the receiver (Pa)
DNI	direct normal irradiation [kW/(m^2·h)]
A_{heli}	area of the heliostat field (m^2)
η_{heli}	efficiency of the heliostat field
d_{month}	number of days of the month (d)

https://doi.org/10.1021/acs.iecr.0c05383
Ind. Eng. Chem. Res. 2021, 60, 7218−7231

h_{sun} number of sun hours with enough irradiation (h)
$MV_{location}$ mean annual production value of the location (MW)
MV_{LV} largest mean annual production value (MW)
$CF_{location}$ correction factor of the location
$n_{tubeTOT}$ total number of tubes

REFERENCES

(1) IDEA. Data and statistic. Available in: https://www.iea.org/statistics/?country=WORLD&year=2016&category=Energy%20supply&indicator=TPESbySource&mode=chart&dataTable=BALANCES (accessed June 11, 2020).
(2) Vasques, T. L.; Moura, P.; de Almeida, A. A review on energy efficiency and demand response with focus on small and medium data centers. *Energy Effic.* **2019**, *12*, 1399−1428.
(3) Eurostat. Statistics Explained. Renewable energy statistics. https://ec.europa.eu/eurostat/statistics-explained/index.php/Renewable_energy_statistics (accessed June 14, 2020).
(4) UN, United Nations. Climate action. https://www.un.org/en/climatechange/ (accessed June 8, 2020).
(5) Carlini, E. M.; Schroeder, R.; Birkebæk, J. M.; Massaro, F. EU transition in power sector: How RES affects the design and operations of transmission power systems. *Electr. Power Syst. Res.* **2019**, *169*, 74−91.
(6) He, Y.-L.; Qiu, Y.; Wang, K.; Yuan, F.; Wang, W.-Q.; Li, M.-J.; Guo, J.-Q. Perspective of concentrating solar power. *Energy* **2020**, *198*, 117373.
(7) Liu, M.; Steven Tay, N. H.; Bell, S.; Belusko, M.; Jacob, R.; Will, G.; Saman, W.; Bruno, F. Review on concentrating solar power plants and new developments in high temperature thermal energy storage technologies. *Renewable Sustainable Energy Rev.* **2016**, *53*, 1411−1432.
(8) Gonzalez Finat, A.; Liberali, R. *Concentrating Solar Power From Research to Implementation*; European Communities: Luxembourg, 2007; pp 1−39.
(9) Martín, L.; Martín, M. Optimal year-round operation of a concentrated solar energy plant in the south of Europe. *Appl. Therm. Eng.* **2013**, *59*, 627−633.
(10) García, S.; Martín, M. Analysis of the performance of Concentrated Solar Power facilities using different thermal fluids. *Chem. Eng. Res. Des.* **2020**, *168*, 46. Rev. Submitted
(11) Fernández, A. G.; Gomez-Vidal, J.; Oró, E.; Kruizenga, A.; Solé, A.; Cabeza, L. F. Mainstreaming commercial CSP systems: A technology review. *Renew. Energy* **2019**, *140*, 152−176.
(12) Hayat, M. B.; Ali, D.; Monyake, K. C.; Alagha, L.; Ahmed, N. Solar energy—A look into power generation, challenges, and a solar-powered future. *Int. J. Energy Res.* **2019**, *43*, 1049−1067.
(13) Zhang, H. L.; Baeyens, J.; Degrève, J.; Cacères, G. Concentrated solar power plants: Review and design methodology. *Renewable Sustainable Energy Rev.* **2013**, *22*, 466−481.
(14) Luceño, J. A.; Martín, M. Two-step optimization procedure for the conceptual design of A-frame systems for solar power plants. *Energy* **2018**, *165*, 483−500.
(15) Luceño, J. A.; Martín, M. Optimal design of aging systems: A-frame coolers design under fouling. *Comput. Chem. Eng.* **2019**, *122*, 47−58.
(16) Heyns, J. A. Performance characteristics of an air-cooled steam condenser incorporating a hybrid (dry/wet) dephlegmator. M.Sc. Thesis, University of Stellenbosch, Stellenbosch, South Africa, 2008.
(17) Sharma, P.; Chandra, L.; Ghoshdastidar, P. S.; Shekhar, R. A novel approach for modelling fluid low and heat transfer in an Open Volumetric Air Receiver using ANSYS-FLUENT. *Sol. Energy* **2020**, *204*, 246−255.
(18) Barreto, G.; Canhoto, P.; Collares-Pereira, M. Parametric analysis and optimisation of porous volumetric solar receivers made of open-cell SiC ceramic foam. *Energy* **2020**, *200*, 117476.
(19) Navalho, J. E. P.; Pereira, J. C. F. A comprehensive and fully predictive discrete methodology for volumetric solar receivers: application to a functional parabolic dish solar collector system. *Appl. Energy* **2020**, *267*, 114781.
(20) Chen, S.; Li, W.; Yan, F. Thermal performance analysis of a porous solar cavity receiver. *Renew. Energy* **2020**, *156*, 558−569.
(21) Gimeno-Furio, A.; Hernandez, L.; Martinez-Cuenca, R.; Mondragón, R.; Vela, A.; Cabedo, L.; Barreneche, C.; Iacob, M. New coloured coatings to enhance silica sand absorbance for direct particle solar receiver applications. *Renew. Energy* **2020**, *152*, 1−8.
(22) Behar, O.; Khellaf, A.; Mohammedi, K. A review of studies on central receiver solar thermal power plants. *Renewable Sustainable Energy Rev.* **2013**, *23*, 12−39.
(23) Pérez Gómez, E. Diseño térmico y análisis económico y medioambiental de una planta termosolar de 30 MW con tecnología de torre central, acumulación de calor mediante sales fundidas y operación ininterrumpida. B.Sc. Thesis, Universidad Carlos III de Madrid, 2013.
(24) Jebamalai, J. S. M. Receiver Design Methodology for Solar Tower Power Plants. M.Sc. Thesis, KTH School of Industrial Engineering and Management, 2016.
(25) Wei, M.; Fan, Y.; Luo, L.; Flamant, G. Fluid Flow distribution optimization for minimizing the peak temperature of a tubular solar receiver. *Energy* **2015**, *91*, 663−677.
(26) Sánchez-González, A.; Rodríguez-Sánchez, M. R.; Santana, D. Aiming factor to flatten the flux distribution on cylindrical receivers. *Energy* **2018**, *153*, 113−125.
(27) Carrizosa, E.; Domínguez-Bravo, C.; Fernández-Cara, E.; Quero, M. Optimization of multiple receivers solar power tower systems. *Energy* **2015**, *90*, 2085−2093.
(28) Alonso-Montesinos, J.; Monterreal, R.; Fernández-Reche, J.; Ballestrín, J.; Carra, E.; Polo, J.; Barbero, J.; Batlles, F. J.; López, G.; Enrique, R.; Martínez-Durbán, M.; Marzo, A. Intra-hour energy potential forecasting in a central solar power plant receiver combining Meteosat images and atmospheric extinction. *Energy* **2019**, *188*, 116034.
(29) Wang, G.; Niu, S.; Yu, S.; Lin, J.; Chen, Z.; Hu, P. Parametric Study on Integrated Thermal and Mechanical Performance of Molten Salt Receiver for Solar Tower Plant. *Int. J. Thermophys.* **2020**, *41*, 23.
(30) Yu, Q.; Fu, P.; Yang, Y.; Qiao, J.; Wang, Z.; Zhang, Q. Modeling and parametric study of molten salt receiver of concentrating solar power tower plant. *Energy* **2020**, *200*, 117505.
(31) Peterseim, J. H.; White, S.; Hellwig, U. Novel solar tower structure to lower plant cost and construction risk. *AIP Conf. Proc.* **2016**, *1734*, 070025.
(32) Wagner, M. J. Simulation and predictive performance modeling of utility-scale central receiver system power plants. M.Sc. Thesis, University of Wisconsin-Madison, 2008.
(33) Mizutani, F. T.; Pessoa, F. L. P.; Queiroz, E. M.; Hauan, S.; Grossmann, I. E. Mathematical programming model for heat exchanger network synthesis including detailed heat exchanger designs. 1. Shell-and-tube heat exchanger design. *Ind. Eng. Chem. Res.* **2003**, *42*, 4009−4018.
(34) TEMA, Tubular Exchanger Manufacturers Association INC. *Standards of the Tube Exchanger Manufacturers Association*, 9th ed.; Gaddis, D., Ed.; Tubular Exchanger Manufacturers Association INC: New York, 2007; pp. 5.1-1−5.2-3.
(35) Drake, T.; Bruce, K.; Frank, B. *Baseload Nitrate Salt Central Receiver Power Plant Design (Final Report)*; Abengoa Solar LLC: Sandia National Lab: Colorado, 2014; pp 1−52.
(36) DWIA, Danish Wind Industry Association. Wind Energy Reference Manual. 2003. http://drømstørre.dk/wp-content/wind/miller/windpower%20web/en/stat/units.htm (accessed February 7, 2020).
(37) Bañuelos-Ruedas, F.; Camacho, C. A.; Rios-Marcuello, S. Methodologies Used in the Extrapolation of Wind Speed Data at Different Heights and Its Impact in the Wind Energy Resource Assessment in a Region. *Wind Farm—Technical Regulation, Potential Estimation and Siting Assessment*; IntechOpen, 2010.
(38) Churchill, S. W.; Chu, H. H. S. Correlating equations for laminar and turbulent free convection from a vertical plate. *Int. J. Heat Mass Tran.* **1975**, *18*, 1323−1329.
(39) White, F. M. Viscous Flow in Ducts. *Fluid Mechanics*, 7th ed.; Mc Graw Hill: New York, 2011, pp 347−453.

https://doi.org/10.1021/acs.iecr.0c05383
Ind. Eng. Chem. Res. 2021, 60, 7218−7231

(40) Zavoico, A. B. *Solar Power: Tower Design Basis Document*, Revision 0; Sandia National Lab: San Francisco, 2001; pp 35−119.
(41) UNEPFI, United Nations Environment Programme Finance Initiative. The GHG Indicator: UNEP Guidelines for Calculating Greenhouse Gas Emissions for Businesses and Non-Commercial Organisations. 2000. https://www.unepfi.org/fileadmin/documents/ghg_indicator_2000.pdf (accessed June 14, 2020).
(42) CDP, Carbon Pricing Connect. October 2017. https://www.cdp.net/en/climate/carbon-pricing/carbon-pricing-connect (accessed July 17, 2020).
(43) SPECIALMETALS. The story of the "INCOLOY® allows series," from 800, through 800H, 800HT®. 2004. https://www.specialmetals.com/assets/smc/documents/alloys/incoloy/incoloy-alloys-800h-800ht.pdf (accessed July 5, 2020).
(44) High Temp Metals. Alloy 800/800AT/800H technical data. 2015. http://www.hightempmetals.com/techdata/hitempIncoloy800data.php (accessed July 5, 2020).
(45) Aesterion Steels LLP. Incoloy 800 Tube, Tubing & Pipe. http://aesteironsteelpipes.com/uns-n08800-incoloy-800-tube-tubing-pipe-258.html#price (accessed 5 July 2020).
(46) Palys, M. J.; Daoutidis, P. Using hydrogen and ammonia for renewable energy storage: A geographically comprehensive techno-economic study. *Comput. Chem. Eng.* **2020**, *136*, 106785.
(47) PVGIS, Photovoltaic Geographical Information System. The European Commission's science and knowledge service, 2020. Available online. https://ec.europa.eu/jrc/en/pvgis (accessed 12 March 2020).
(48) Martín, J. H. Diseño y análisis de una planta termosolar de torre central con configuraciones de único o doble receptor operando con sales fundidas. B.Sc. Thesis, Universidad Carlos III de Madrid, 2012.

https://doi.org/10.1021/acs.iecr.0c05383
Ind. Eng. Chem. Res. 2021, 60, 7218−7231